Temporal Variations of Titan's Middle-Atmospheric Temperatures From 2004-2009 Observed by Cassini/CIRS

Richard K. Achterberg[a], Peter J. Gierasch[b], Barney J. Conrath[b], F. Michael Flasar[c], Conor A. Nixon[a]

[a]*University of Maryland, Department of Astronomy, College Park, MD 20742*
[b]*Department of Astronomy, Cornell University, Ithaca, NY 14853*
[c]*NASA Goddard Space Flight Center, Greenbelt, MD 20771*

Submitted to *Icarus* 13 May 2010
Revised July 5, 2010
Accepted AUG 2010

Pages: 46

Figures: 14

Tables: 2

Email address: Richard.K.Achterberg@nasa.gov (Richard K. Achterberg)

Proposed Running Head: Time Variation of Titan's Stratospheric Temperatures

Editorial correspondence to:

Dr. Richard K. Achterberg

NASA Goddard Space Flight Center

Code 693.0

Greenbelt, MD 20771

Phone: 301-286-1550

Fax: 301-286-0212

Email: Richard.K.Achterberg@nasa.gov

Abstract

We use five and one-half years of limb- and nadir-viewing temperature mapping observations by the Composite Infrared Radiometer-Spectrometer (CIRS) on the Cassini Saturn orbiter, taken between July 2004 and December 2009 (L_S from 293° to 4°; northern mid-winter to just after northern spring equinox), to monitor temperature changes in the upper stratosphere and lower mesosphere of Titan. The largest changes are in the northern (winter) polar stratopause, which has declined in temperature by over 20 K between 2005 and 2009. Throughout the rest of the mid to upper stratosphere and lower mesosphere, temperature changes are less than 5 K. In the southern hemisphere, temperatures in the middle stratosphere near 1 mbar increased by 1 to 2 K from 2004 through early 2007, then declined by 2 to 4 K throughout 2008 and 2009, with the changes being larger at more polar latitudes. Middle stratospheric temperatures at mid-northern latitudes show a small 1 to 2 K increase from 2005 through 2009. At north polar latitudes within the polar vortex, temperatures in the middle stratosphere show a $\sim$ 4 K increase during 2007, followed by a comparable decrease in temperatures in 2008 and into early 2009. The observed temperature changes in the north polar region are consistent with a weakening of the subsidence within the descending branch of the middle atmosphere meridional circulation.

Key words: Titan, atmosphere, Atmospheres, structure, Atmospheres, dynamics, Infrared Observations

1. Introduction

With an obliquity of approximately 26.7°, there are strong seasonal variations of the insolation of Titan's atmosphere. Although the radiative timescales in the troposphere are longer than the Titan year (Smith et al., 1981), in the mid-stratosphere and above the radiative response time becomes short enough that seasonal variations in temperature, and thus dynamics, are expected (Flasar et al., 1981).

The earliest measurements of Titan's atmospheric temperatures were from the Voyager 1 infrared spectrometer IRIS, which observed Titan in early northern spring ($L_S \approx 9°$). Retrievals of temperatures at 0.4 and 1 mbar by Flasar and Conrath (1990) showed a hemispheric asymmetry, with temperatures near 60° N approximately 15 K colder than equatorial and low southern latitudes, with a smaller drop of about 5 K at 60° S. This temperature asymmetry is somewhat larger than expected given radiative cooling timescales at these levels of about 1 Earth year (one Titan year is 29.5 Earth years). Flasar and Conrath (1990) proposed that, because of the coupling of the temperatures and winds through gradient wind balance, the temperatures respond to the solar forcing on the longer dynamical timescale on which the meridional circulation transports zonal momentum between hemispheres. Alternately, Bézard et al. (1995) suggested that the temperature asymmetry is the result of hemispheric asymmetries in the opacity sources responsible for solar heating and radiative cooling. Stratospheric temperature retrievals from Cassini Composite Infrared Spectrometer (CIRS) data taken around northern mid-winter (Flasar et al., 2005; Achterberg et al., 2008a), showed a somewhat stronger asymmetry, with 1 mbar temperatures poleward of 60° N 20-30 K colder than the equator. The most remarkable result from the CIRS temperature data is the discovery that the stratopause was over 20 K warmer and over a scale height in altitude higher at high northern winter latitudes than at the equator (Achterberg et al., 2008a). As the winter stratopause is high enough in altitude to be above the polar shadow, and there is an increased haze opacity in the winter polar hood (Smith et al., 1981), increased radiative heating may contribute to the warm stratopause. Another possibility suggested by Achterberg et al. (2008a) is adiabatic heating in the descending branch of the meridional circulation. Subsidence has also been invoked to explain the enhanced abundance of nitriles and some hydrocarbons seen at high northern latitudes by Voyager and Cassini (Rannou et al., 2004; Lebonnois et al., 2009; Teanby et al., 2009).

With five and a half years of data now available from Cassini, covering just over two-thirds of a season from early northern winter to just after northern spring equinox (L_S from 293° to 4°), we have used both nadir and limb viewing temperature mapping observations from CIRS to look for temporal changes in temperature in the upper stratosphere and lower mesosphere. Section 2 describes the data sets used and the temperature retrieval procedure. Section 3 presents the observed time variations of the retrieved temperatures and of the zonal mean gradient winds consistent with the temperatures. Section 4 compares the observations with the earlier Voyager observations and with general circulation models of Titan, and discusses the implications of the observations for the mean meridional circulation.

2. Observations and Data Analysis

To obtain temperatures in the upper stratosphere, we use thermal infrared spectra from focal plane 4 (FP4) of CIRS, which covers the spectral range from 1100 to 1400 cm^{-1} with a spectral resolution adjustable between approximately 0.5 and 15.5 cm^{-1}. FP4 is a 10-element linear array, each pixel of which has a square field of view of 0.28 mrad. The instrument and its operation is described in detail by Flasar et al. (2004). The data used cover the time period from the T0 flyby on 2 July 2004 ($L_S = 293°$), just after orbit insertion, through the T63 flyby on 11 December 2009 ($L_S = 4°$), just after Titan's northern spring equinox.

Two types of temperature mapping observations are used: nadir-viewing maps which usually cover the visible hemisphere of Titan, and limb-viewing maps which provide better altitude coverage than nadir-viewing observations, but which cover only a single longitude for each observation. For the nadir-viewing maps, a series of continuous slews, perpendicular to the 1x10 FP4 array, are used to cover the visible disk from a spacecraft distance of 250,000 to 400,000 km, giving a spatial resolution of 1.5° to 2.5° of arc at disk center, and the data is taken at a spectral resolution of $2.8\,\mathrm{cm}^{-1}$. A list of the nadir observations is given in Table 1. For the limb-viewing maps, the array is placed perpendicular to the limb of Titan, with two separate vertical placements of the array, one above the other with an approximately 3 pixel overlap. Data are taken every 5° in latitude over a roughly 90° latitude range. At each position of the array, 10 to 12 spectra are acquired in each detector at a spectral resolution of $15.5\,\mathrm{cm}^{-1}$, and are averaged together to improve the signal-to-noise ratio. Spectra taken during the slews between array positions are ignored. The limb maps are taken at a range of about 120,000 km, giving a vertical spatial resolution of about 40 km, somewhat less than the pressure scale height in the stratosphere. A list of the limb observations used is given in Table 2. The latitude and time coverage provided by both sets of observations is shown in Fig. 1.

Temperatures are retrieved from the observed spectra using the procedure described in detail by Achterberg et al. (2008a); only a very brief summary is provided here. For the nadir maps, temperatures are retrieved from individual spectra by a constrained linear inversion algorithm (Conrath et al., 1998), using the spectral range from 1251 to $1311\,\mathrm{cm}^{-1}$ within the P and Q branches of the ν_4 band of CH_4. The forward model uses 200 layers, equally spaced in log-pressure between 1456 and 0.001 mbar. CH_4 ν_4 band absorption is calculated using the correlated-k approximation (Lacis and Oinas, 1991), with line data taken from the 2003 release of the GEISA line atlas (Jacquinet-Husson et al., 2005), assuming a stratospheric mole fraction of 0.0141 (Niemann et al., 2005). The retrieved temperatures are valid between roughly 0.2 and 8 mbar, except at north polar latitudes where the region of validity shifts to approximately 0.1 mbar to 2 mbar because of the warmer upper stratosphere and colder middle and lower stratosphere. Outside of the pressure range that is strongly constrained by the data, the retrieved temperatures relax to the initial guess profile.

For the limb maps, the large vertical extent of the atmosphere relative to the radius of Titan requires the use of a 2-dimensional retrieval algorithm (Achterberg et al., 2008a), in which all of the data from a single map is used simultaneously to retrieve the temperature and aerosol abundance as a function of both latitude and altitude, assuming no variations with longitude, as well as altitude pointing corrections. The spectral range used 1210 to 1315 cm^{-1}. The forward model uses 200 layers equally spaced in altitude between the surface and 550 km, and latitude points spaced every 5°, with the latitude boundaries dependent upon the latitude range of the data used. Again, CH_4 absorption is included using the correlated-k approximation, and haze absorption is also included using a gray absorber with no scattering. The retrieved temperatures are valid between approximately 0.005 and 5 mbar, except northwards of about 60° N where they are valid between about 0.005 and 2 mbar. For both sets of retrievals, the initial guess for the retrievals was the latitude-dependent, smoothed, time- and zonally-averaged temperature cross section of Achterberg et al. (2008a, Fig. 9).

3. Results

Figure 2 illustrates the large-scale changes in Titan's stratospheric thermal structure between the early part of the Cassini mission (northern mid-winter) and the period just before northern spring equinox. Cross-sections of zonal mean temperatures averaged over flybys T0 through T13 (July 2004 through March 2006) are shown in the top panel, and over T45 through T63 (July 2008 through December 2009) in the bottom panel. The averages were constructed by averaging both the nadir- and limb-viewing data in 5° latitude bins, and smoothing the resulting averages by 3 applications of a sliding 10° rectangular window. The middle panel shows the change in temperature between the early and late temperature averages. The largest changes in temperature occur at around 60° N, near the northern boundary of the winter polar vortex, with only small changes in the southern hemisphere. The most prominent change is a strong cooling of the warm winter polar stratopause by $\approx$ 20K, along with a general cooling of the stratopause and lower mesosphere. In the mid-stratosphere, temperature changes are smaller than in the lower mesosphere, with warming of 2-3K in the northern hemisphere and weak cooling in the southern hemisphere.

3.1. Limb Maps: Lower Mesosphere and Stratopause

Figure 3 shows a time sequence of temperature cross-sections from individual limb maps with northern hemisphere coverage. The dashed line on the figure indicates the stratopause, calculated as the pressure where the temperature is a local maximum at each latitude. The warm, elevated north polar stratopause has been cooling from 2005 through 2009 at a rate of about 5 K per year. In addition, the transition between the $\sim$ 0.1 mbar near-equatorial stratopause and the elevated polar stratopause has become much more abrupt, and in the T59 and T63 maps (L_S = 359° and L_S = 4°), the stratopause has essentially dissappeared at northern midlatitudes, with the temperatures profile becoming nearly isothermal for pressures less than about 0.3 mbar.

Figure 4 shows a time sequence of equatorial temperature cross-sections from individual limb maps. From 2005 through 2007, changes to the temperature structure are small. From late 2007 through mid 2009, temperatures in the lower mesosphere between about 0.1 and 0.01 mbar decrease by approximately 5 K, accompanied by a shift in the stratopause to higher pressures.

Figure 5 shows a time sequence of southern hemisphere temperature cross-sections from individual limb maps. Coverage of high southern latitudes from the limb maps is unfortunately sparse (see Fig. 1). Little evidence of temperature changes can be seen, apart from indications of cooling in the lower mesosphere at higher latitudes, and the disappearance of the slight elevation of the stratopause at south polar latitudes.

3.2. Nadir Maps: Middle Stratosphere

To examine the temporal variations in the middle stratosphere, temperatures retrieved from the nadir maps for each flyby were zonally averaged in 5° wide latitude bins. In calculating the averages, the variation of latitude along the observed ray paths, which is significant because of the large vertical extent of Titan's atmosphere, was taken into account. Figure 6 shows a time series of the zonal mean temperatures at 1 mbar for a representative set of latitudes. Unfortunately, flyby geometries did not allow for good nadir views of latitudes poleward of approximately 60° N or 70° S for the first two years of the mission, except for the south pole on the T0 flyby immediately after orbit insertion.

The north polar data at 75° N and 85° N indicate a temperature increase of ~ 3 K between early 2007 and early 2008, but a similar decrease from early 2008 through spring equinox, despite increasing sunlight in the north polar region as spring approaches. The mid-northern hemisphere temperatures (30° N - 60° N) show considerable scatter, but indicate a temperature increase of 2 to 3 K from 2005 to 2009, consistent with the larger time averages shown in Fig. 2. Near equatorial temperatures are constant over the time of the observations. At mid-to-high southern latitudes, temperatures increased by about 1 K between mid-2004 and early 2007; there is then clear temperature decrease beginning in late 2007, with the amplitude of the decrease from late 2007 to mid-2009 varying from ~ 1 K around 45° S to ~ 4 K near the south pole.

3.3. Zonal Winds

Using the assumption of gradient wind balance – that the meridional pressure gradient is balanced by the horizontal component of the the sum of the Coriolis and centrifugal forces, which is expected to hold for Titan – the zonal wind velocity u is related to the meridional gradient of the temperature T by

$$\frac{\partial}{\partial z_{\|}}\left(2\Omega u + \frac{u^2}{rcos\phi}\right) = -\frac{g}{T}\frac{1}{r}\left(\frac{\partial T}{\partial \phi}\right)_p . \qquad (1)$$

Here Ω is Titan's rotation frequency, ϕ is latitude, g is gravitational acceleration, and for a thick atmosphere, the "vertical" derivative $\partial z_{\parallel}$ is taken along the direction parallel to the rotation axis (Flasar et al., 2005). To minimize the noise from taking derivatives of the temperature field, and to get full latitude coverage, Eq. 1 is applied to the averaged temperature fields of Fig. 2. Following Achterberg et al. (2008a), we use as a boundary condition a wind in solid body rotation at 10 mbar with an angular velocity of four times the solid body rotation rate, consistent with the winds at that level measured by the Huygens Doppler Wind Experiment (Bird et al., 2005; Folkner et al., 2006).

The resulting winds are shown in Fig. 7, along with the change in the wind between the early and late averages. Changes in the southern hemisphere winds are small, as expected from the small changes in the southern hemisphere temperatures. The main change in the winds between 2005 and 2009 is an extension of the strong winter hemisphere jet to higher altitudes; the weakening meridional temperature gradients at the latitude of the jet correspond to a slower decay of the jet with increasing altitude.

3.4. Stratospheric Pole Offset

Analysis of mid-stratospheric temperatures by Achterberg et al. (2008b) showed that zonal variations of temperature were dominated by a zonal wavenumber 1 feature which was stationary in either a solar-fixed or stellar-fixed reference frame to within the observational uncertainty. The meridional structure of the wavenumber 1 feature was consistent with Titan's stratospheric temperatures and winds being symmetric about an axis that is offset from the then-current IAU definition of Titan's solid body rotation axis by $4.1° \pm 0.2°$, with the north pole tilted towards a direction $76° \pm 2°$ west of the subsolar longitude. Subsequently, similar offsets were discovered in the symmetry axis of the hemispheric north-south haze asymmetry (Roman et al., 2009) and of the HCN abundance (Teanby et al., 2010).

Recent GCM simulations by Tokano (2010) produce a stratospheric atmospheric angular momentum (AAM) vector which is offset from the rotation pole by a few degrees and which precesses westward with a period of one Titan solar day, as a result of forcing by solar thermal tides. These results are broadly consistent with the observations, except that the AAM vector in the GCM simulations is tilted toward the anti-solar longitude in northern winter. Tokano (2010) also found that the angle of the AAM tilt in the GCM varies strongly with season, with a maximum tilt amplitude occurring after the solstices and the tilt becoming near zero shortly after equinox, with the tilt angle in the mid-stratosphere dropping by ~30% to 50% over the period of the CIRS observations.

To look for temporal variations of the stratospheric tilt, the procedure described by Achterberg et al. (2008b) for fitting the symmetry axis of the temperature field was applied to the retrieved 1 mbar temperature maps for each Titan flyby. The results are shown in Fig. 8 in both sun-fixed and inertial (star-fixed) reference frames. The error bars shown are 1-σ uncertainties resulting from uncertainties in the retrieved temperatures. Navigation of support imaging for the earliest Titan temperature maps indicated uncertainties in the reconstructed pointing data of one-third to one-half of a CIRS FP4 field of view, and retrieved pointing corrections from the limb retrievals are also in general one-third of a field of view or less, corresponding to errors of about 1° of arc on Titan. As the pointing errors will be moderately strongly correlated over a temperature mapping observation, it is likely that much of the considerable scatter in Fig. 8 is from pointing errors.

Despite the scatter, the amplitude of the fitted pole offset shows no indication of having decreased over the period of the observations as predicted by the model of Tokano (2010); if anything the data suggest a slight increase in the amplitude of the tilt. Linear fits to the azimuth angle of the tilt as a function of time, shown as dotted lines in Fig. 8, suggest that the tilt is closer to stationary in the inertial reference frame than in the solar reference frame; the fitted long-term drift rates of the azimuth are $(29 \pm 8) \times 10^{-8}\,\mathrm{deg\,s^{-1}}$ in the sun-fixed frame and $(3.5 \pm 7.9) \times 10^{-8}\,\mathrm{deg\,s^{-1}}$ in the inertial frame. The plots of tilt azimuth also show an apparent oscillation with a period of about 3 years. Calculation of a Lomb-Scargle periodogram (Press and Teukolsky, 1988) from the tilt azimuth data in the inertial frame gives a maximum signal at a period of 2.73 Earth years, with a false alarm probability of 11.5% (i.e. statistically significant at the 88.5% level). With the large scatter in the tilt data, and the correspondingly low statistical significance of the results, further data to be obtained during the Cassini Solstice Mission are needed to clearly determine the behavior of the stratospheric pole offset.

4. Discussion

4.1. Comparison with Voyager 1 IRIS

Prior to Cassini, the only measurements of meridional temperature profiles on Titan were from the Infrared Interferometer Spectrometer (IRIS) on Voyager 1 (Flasar et al., 1981; Flasar and Conrath, 1990; Coustenis and Bézard, 1995), which flew by Titan in November 1980, during early northern spring ($L_S = 9°$). Figure 9 shows the 0.4 mbar and 1.0 mbar temperatures retrieved from Voyager 1 IRIS by Flasar and Conrath (1990), along with temperatures at the same pressures retrieved from CIRS data from flybys T45 through T59 (July 2008 to July 2009, $L_S = 347° - 359°$), taken slightly less than one Titan year after the IRIS data. Overall, the two data sets are consistent with each other, with two main differences. First, the Voyager data show an indication of the meridional temperature gradient becoming steeper at 60° S, which is not seen in the CIRS data, but which is consistent with the the Voyager data being taken in early southern spring, while the Cassini data is from late southern winter. Secondly, the Voyager data are somewhat colder at the equator at 0.4 mbar than the CIRS data.

4.2. Comparison with Titan General Circulation Models

The primary objective of Titan general circulation modeling is to contribute to an understanding of the processes that control the structure and dynamics of the atmosphere. This modeling objective can only be met through the comparison of model predictions with the available measurements of the spatial structure and temporal evolution of atmospheric temperatures, wind fields, gas abundances, and aerosols. By adjusting parameterizations and systematically introducing new mechanisms, the relative importance of various processes can be established. The Cassini mission has obtained a wealth of new information on Titan's atmosphere that can establish important constraints. Although the fraction of the Titan seasonal cycle covered thus far by CIRS observations is limited (L_S from 293° through 4°), temporal changes in the temperature field (Fig. 2) and the associated gradient thermal wind field (Fig. 7) are clearly evident. These results can now be compared with circulation model predictions.

In an early pioneering effort, a 3-D model derived from a terrestrial GCM was developed at the Laboratoire de Météorologie Dynamique (LMD). With a top at $\sim$ 0.3 mbar, the optically active gases and haze production rates were held fixed, independent of latitude and time (Hourdin et al., 1995). Results were presented for northern winter solstice ($L_s = 270°$) and northern spring equinox ($L_s = 360°$). Although the height range covered by the model limits the comparisons that can be made with the CIRS middle atmosphere results, the predicted gross seasonal changes in the 0.3 - 10 mbar region are qualitatively similar to those observed. However, the model underestimated the latitudinal temperature gradients and the strength of the winter hemisphere jet.

Subsequently, Tokano et al. (1999) constructed a Titan GCM in which an attempt was made to include the effects of seasonally varying haze opacity within the framework of a simplified model. The potential importance of a time and spatially varying haze opacity was established, although resulting temperature gradients in latitude in the lower stratosphere were generally weaker than observed. The top of the model was at $\sim$ 0.1 mbar so direct comparisons with CIRS results in the upper stratosphere cannot be made. Friedson et al. (2009) have also developed a fully three-dimensional Titan GCM, based upon the NCAR Community Atmosphere Model 3.0, including detailed calculations of surface-atmosphere interactions and radiative transfer, but with the assumption that the radiatively active gases and aerosols were uniform in latitude and time. Their model produced stratospheric winds with a maximum amplitude of $\sim 12\,\mathrm{m\,s^{-1}}$, and equator-to-pole temperature gradients of $\sim 1\,\mathrm{K}$, much less than observed.

More recently, the LMD group and their collaborators have developed and continued to refine a zonally symmetric model with interactive dynamics, radiative transfer, photochemistry, and cloud micro-physics (Lebonnois et al., 2001, 2003; Hourdin et al., 2004; Rannou et al., 2004). Horizontal transport by barorotropic eddies is parameterized in the 2-dimensional model using the results of Luz and Hourdin (2003) and Luz et al. (2003). Haze transported to the polar regions is found to have a major effect on the radiative heating and cooling rates resulting in enhanced net radiative cooling, especially at high latitudes in the winter hemisphere. Consequently, equator-to-pole temperature gradients are increased with a corresponding strengthening of the wind field. Here we make use of a publicly-available database of output from this model (Rannou et al., 2005, http://www.lmd.jussieu.fr/titanDbase/index.hml).

Results from the model have previously been compared with CIRS-derived thermal structure, zonal winds, and stratospheric gas distributions for $L_s \sim 300°$ by Crespin et al. (2008). We can now extend the comparison of the temperature and zonal wind field through $L_s \sim 360°$ with emphasis on the temporal changes. Zonal mean meridional temperature and zonal wind cross sections from the model for $L_s = 309°$ and 358° are shown in Fig. 10, along with the changes over this time interval. These results can be compared with the CIRS retrieved temperatures and winds and their changes shown in Figs. 2 and 7. The model-predicted temperature and wind cross sections agree qualitatively with the measurements, with a strong temperature maximum in the upper levels at high northern latitudes and a strong mid latitude jet in the winter hemisphere. However, notable quantitative differences exist. The model temperature maxima for both time periods are somewhat warmer and occur at higher pressures than found in the measurements. Crespin et al. (2008) suggest that this may be due at least in part to placement of the modeled aerosol production source too deep in the atmosphere. In addition, the measurements indicate a significant increase in the stratopause altitude between the equator and the north polar region for both times, a feature that is not captured by the model. The measurements show a temporal decrease in temperature in the upper atmospheric levels at high northern latitudes with the greatest change occurring at the temperature maximum centered near 0.01 mbar. The model results indicate little change in the maximum with some increase in temperature at the equatorward edge of the warm region. Both the measurements and the model show an increase in zonal wind speed at mid and low latitudes, although the spatial extent and magnitude of the change differs considerably between the two.

4.3. Potential Vorticity and Stability of the Polar Vortex

The Ertel potential vorticity and the potential temperature (a function of the entropy) are materially conserved quantities in adiabatic inviscid flow. In a flow that is also axisymmetric, the zonal mean angular momentum about the symmetry axis is also conserved. The zonal mean cross sections of these three quantities are thus of particular interest as tracers of the meridional circulation, or as indicators of the strength of non-adiabatic effects (radiation, for example) or of wave and eddy forcing. The seasonal changes of these three quantities should reveal the forcing that drives the general circulation.

As explained in section 3.3, the retrieved temperatures can be used to make estimates of the zonal wind. The potential temperature can be calculated from the temperature, the angular momentum from the wind, and finally the potential vorticity can be calculated from the wind and the potential temperature. These steps were carried out as described in Achterberg et al. (2008a). The resulting meridional cross sections are displayed in Figs. 11 through 13, as calculated from the temperatures and winds from Fig. 2 and Fig. 7, respectively.

Noise is magnified when the retrieved temperatures are differentiated. This has a strong effect on the potential vorticity, because two spatial derivatives are taken. Moreover, it is the gradients of the field that are of interest in interpretations, such as baroclinic instability assessment. To reduce noise as much as possible when generating these conserved quantities, we smoothed spatially, typically with three passes of a sliding box average ten degrees of latitude in width. In addition, we evaluated temporal change by using all four time bins and fitting a linear rate of change to each (latitude, pressure) point in the meridional plane. This procedure uses all the data, and captures the important time dependence, since only a fraction of a season is available at present.

The angular momentum per unit mass (Fig. 12) is dominated by the zonal mean wind, with only a minor contribution from the planetary rotation. Consequently, the angular momentum distribution is very similar to the wind field, with closed contours in the middle stratosphere. The potential vorticity cross sections (Fig. 13) show a monotonic increase from the south pole through approximately 65° N, on the poleward flank of the winter polar vortex, where there is a maximum in the potential vorticity, and then a descrease toward the north pole, where there is a local minimum. This local maximum in the potential vorticity should be viewed with caution; it is near the edge of the domain and is sensitive to the smoothing approach. Nevertheless, it consistently appears in all four of our time bins, and the amplitude of the maximum shows an increase as time advances.

There has been only limited investigation of stability criteria for nongeostrophic vortex flows. It is known that if the Ertel potential vorticity changes sign within a vortex, or if the angular momentum per unit mass decreases with distance from the rotation axis along a surface of constant potential temperature, then the flow is unstable to symmetric or inertial overturning (Eliassen, 1951). The Titan cross sections displayed in Figs. 12 and 13 do not do this. In quasigeostrophic flow, a necessary, but not sufficient, condition for barotropic or baroclinic instabilities is a change in sign of the meridional gradient of the potential vorticity (e.g. Pierrehumbert and Swanson, 1995). In the cyclostrophic case a stability analysis has been carried out by Montgomery and Shapiro (1995), giving the same result, but the structure of perturbations is limited to low wavenumbers and therefore the conclusion is not general. The local maximum in potential vorticity would thus suggest that the polar vortex may be unstable, although it is possible that the polar vortex is stabilized by geometry or stratification.

4.4. Implications for the Zonal Mean Meridional Circulation

On Earth, the radiative relaxation time, τ_r, is roughly comparable in the troposphere and middle atmosphere, approximately a few days (see e.g. Houghton, 1977; Fels, 1982; Andrews et al., 1987). In Titan's atmosphere the range is much larger. Figure 14 shows order-of-magnitude estimates of the radiative cooling timescales at equatorial (5° S) and north polar (75° N) latitudes, calculated using the Newtonian cooling and raditation-to-space approximations (Flasar et al., 1981; Andrews et al., 1987, section 2.5.2) with cooling from CH_4, C_2H_2 and C_2H_6. Gas abundances were assumed constant with altitude, using the CH_4 mole fraction from Niemann et al. (2005), and C_2H_2 and C_2H_6 mole fractions from table 2 of Coustenis et al. (2010). Because of the lack of other trace gases and of aerosols, the cooling times in Fig. 14 will be overestimated somewhat (see Tomasko et al., 2008), but the differences between the polar regions and the equator due to the temperature differences should be qualitatively correct.

In the lower troposphere $\tau_r \sim 10^9 - 10^{10}\,\mathrm{s}$ ($\sim$ 100 terrestrial years or $\sim$ 3 Titan years, Smith et al., 1981; Strobel et al., 2009). It decreases with altitude to $\sim 10^7\,\mathrm{s}$ at 1 mbar in the stratosphere at equatorial and summer latitudes (Fig. 14) and decreases more slowly with height above that level. The slower decrease results from the compensation of the decrease in atmospheric mass per scale height with altitude, which acts to decrease τ_r, and the decreased emissivity of the principal hydrocarbon coolants with altitude, which acts to increase it. The variation is more extreme at high latitudes in the winter hemisphere. The cold temperatures near 1 mbar imply relaxation times $\sim 10^8$ s, comparable to a Titan season, and near the high-latitude warm stratopause $\tau_r \sim 10^6$ s, comparable to one Titan day. Hence, the winter stratopause region should have observable diurnal effects, but the paucity of longitude coverage from the limb scans (Achterberg et al., 2008a), which are needed to sound these high altitudes, hamper attempts to see the variation.

The large variation of τ_r in the middle atmosphere has implications for the structure of the zonal-mean meridional circulation. To see this, consider the zonally-averaged heat equation (e.g. Achterberg et al., 2008a):

$$\frac{\partial T}{\partial t} \approx -w\left(\frac{\partial T}{\partial z} + \frac{g}{C_p}\right) - \frac{T - T_{eq}}{\tau_r}, \tag{2}$$

where w is the vertical velocity, C_p is the heat capacity at constant pressure, and T_{eq} is the radiative-equilibrium temperature. All variables are zonal averages. Eq.(2) says that the rate of temperature change is equal to the adiabatic heating and cooling associated with descent and ascent, plus diabatic heating and cooling, parameterized as a Newtonian relaxation of the temperature T to T_{eq} over the time scale τ_r. The balance neglects the meridional advection of heat. For cyclostrophic flow, the ratio of this to the vertical advection term in (2) is small, $1/Ri$, where $Ri \sim 5$ is the Richardson number in Titan's middle atmosphere (Flasar and Conrath, 1990). In the absence of motion, (2) reduces to a purely radiative response, T_r:

$$\frac{\partial T_r}{\partial t} \approx -\frac{T_r - T_{eq}}{\tau_r}. \tag{3}$$

Combining (2) and (3) yields

$$\frac{\partial (T - T_r)}{\partial t} \sim -w\left(\frac{\partial T}{\partial z} + \frac{g}{C_p}\right) - \frac{T - T_r}{\tau_r}. \tag{4}$$

Casting both the temporal change and diabatic heating/cooling in terms of $T - T_r$

permits a straightforward comparison of the two. The ratio of the time derivative to the radiative term is $\Omega_s \tau_r$, where Ω_s is Titan's (and Saturn's) seasonal frequency: $2\pi/29.5$ Earth years. With the exception of the cold region below the 1 mbar level at high northern latitudes in winter, $\Omega_s \tau_r \ll 1$, and the radiative term is much larger. Hence the dominant balance in (4) is:

$$w\left(\frac{\partial T}{\partial z} + \frac{g}{C_p}\right) \approx -\frac{T - T_r}{\tau_r}. \tag{5}$$

The adiabatic heating and cooling associated with vertical motion keeps the atmospheric temperature from relaxing to a purely radiative solution. This is most evident at high northern latitudes near the stratopause level (Achterberg et al., 2008a), where subsidence maintains a temperature, $T \sim 200\,\mathrm{K}$, that is much higher than the radiative solution, $T_r \sim 100\,\mathrm{K}$ (Hourdin et al., 1995): $T - T_r \sim 100\,\mathrm{K}$. At the 0.01 mbar level $\tau_r \approx 1 \times 10^6\,\mathrm{s}$ (Fig. 14), and the static stability, $\left(\frac{\partial T}{\partial z} + \frac{g}{C_p}\right) \sim 1\,\mathrm{K/km}$, taking $\partial T/\partial z \approx 0$. From (5), this implies a subsidence of 10 cm/s, large by Titan standards. At low and southern latitudes, $T - T_r$ is much smaller, $\sim 10\,\mathrm{K}$, and $\tau_r \approx 4 \times 10^6\,\mathrm{s}$. Hence the relaxation term on the right-hand side of (5) is ~ 40 times smaller than near the north pole at low and southern latitudes. As the static stability at these altitudes does not vary that much with latitude, the upwelling leg of the meridional circulation is typified by vertical velocities $< 1\,\mathrm{mm\,s^{-1}}$. Mass continuity requires that the area weighted average of the vertical velocities over latitude vanish, ignoring the possibility of hydrodynamic escape over much longer time scales (see, e.g., Strobel, 2009). It follows that the area of subsidence near 0.01 mbar in the north is relatively compact, more than a factor of 10 smaller than the area of ascent at low and southern latitudes.

Much lower in the stratosphere at high northern latitudes, $\Omega_s \tau_r \sim 1$, which is much larger than elsewhere in the middle atmosphere, and all the terms in (4) are required to account for the balance. Rannou et al. (2004) have emphasized the importance of aerosol transport to high latitudes in the winter hemisphere and the enhanced cooling that can result. However, the neglect of aerosols in our estimate of τ_r may not be critical for the colder temperatures in the lower stratosphere, because of the extreme sensitivity of τ_r to temperature. Once τ_r becomes comparable to seasonal time scales, temperatures at high latitudes in the winter and early spring cannot decline much further, because the sun comes back too soon to warm up the polar region after the winter night.

The 1-mbar temperatures at 75° N and 85° N exhibit a curious behavior in late winter (Fig. 6). They increase between $L_S = 330°$ and $340°$, and decrease between $L_S = 340°$ and $360°$. The increase could plausibly be explained by warming from the sun as the shadow of the polar night recedes. The subsequent decrease, however, may reflect the interplay between solar heating and adiabatic heating from subsidence in the polar region. Evidence that the subsidence, inferred near the stratopause in the retrieved temperature cross sections (Fig. 2), actually extends down to the 1 mbar level comes from a consideration of the retrieved distribution of organic compounds aside from CH_4 in the middle atmosphere. The retrieved distribution of these gases at high northern latitudes shows enhancements down to the 1 mbar level and lower (Teanby et al., 2008; Coustenis et al., 2007). They are mostly formed from photolytic, catalytic and electron-impact dissociation of N_2 and CH_4 high in the atmosphere, and they condense in the the lower stratosphere or tropopause region. The mean concentration of the organic molecules therefore increases with altitude in the middle atmosphere, and subsidence at high northern latitudes will produce higher concentrations along isobars (see e.g. Teanby et al., 2009). If the 1-mbar temperature is maintained by radiative heating and cooling and adiabatic warming from subsidence, the observed cooling between $L_S = 340°$ and $360°$ may signal a weakening in the subsiding leg of the meridional circulation at this level. If the weakening is rapid enough, it could offset the enhanced warming from the sun as it rises higher in the sky.

Acknowledgements

We thank Todd Ansty for implementation of the pointing commands for many CIRS Titan observations; Emannuel Lellouch for implementing the internal CIRS command tables for the Titan observations; Marcia Segura, Shane Albright, Jim Tingley, Monte Kalberer, Paul Romani, Amy Simon-Miller, Gordy Bjoraker and Matt Elliott for their work in getting the CIRS commands to the spacecraft and the returned data on to the CIRS data server; and Don Jennings, Virgil Kunde, Ron Carlson, Andrei Mamoutkine, Ever Guandique, Nicolas Gorius and John Brasunas for CIRS data calibration. This work was supported by the NASA Cassini Project.

References

Achterberg, R. K., Conrath, B. J., Gierasch, P. J., Flasar, F. M., Nixon, C. A., 2008a. Titan's middle-atmospheric temperatures and dynamics observed by the Cassini Composite Infrared Spectrometer. Icarus 194, 263–277.

Achterberg, R. K., Conrath, B. J., Gierasch, P. J., Flasar, F. M., Nixon, C. A., 2008b. Observation of a tilt of Titan's middle-atmospheric superrotation. Icarus 197, 549–555.

Andrews, D. G., Holton, J. R., Leovy, C. B., 1987. Middle Atmosphere Dynamics. Academic Press, Orlando.

Bézard, B., Coustenis, A., McKay, C. P., 1995. Titan's stratospheric temperature asymmetry: A radiative origin? Icarus 113, 267–276.

Bird, M. K., Allison, M., Asmar, S. W., Atkinson, D. H., Avruch, I. M., Dutta-Roy, R., Dzierma, Y., Edenhofer, P., Folkner, W. M., Gurvits, L. I., Johnston, D. V., Plettemeier, D., Pogrebenko, S. V., Preston, R. A., Tyler, G. L., 2005. The vertical profile of winds on Titan. Nature 438, 800–802.

Conrath, B. J., Gierasch, P. J., Ustinov, E. A., 1998. Thermal Structure and Para Hydrogen Fraction on the Outer Planets from Voyager IRIS Measurements. Icarus 135, 501–517.

Coustenis, A., Bézard, B., 1995. Titan's atmosphere from Voyager infrared observations. 4: Latitudinal variations of temperature and composition. Icarus 115, 126–140.

Coustenis, A., Achterberg, R. K., Conrath, B. J., Jennings, D. E., Marten, A., Gautier, D., Nixon, C. A., Flasar, F. M., Teanby, N. A., Bézard, B., Samuelson, R. E., Carlson, R. C., Lellouch, E., Bjoraker, G. L., Romani, P. N., Taylor, F. W., Irwin, P. G. J., Fouchet, T., Hubert, A., Orton, G. S., Kunde, V. G., Vinatier, S., Mondellini, J., Abbas, M. M., Courtin, R., 2007. The composition of Titan's stratosphere from Cassini/CIRS mid-infrared spectra. Icarus 189, 35–62.

Coustenis, A., Jennings, D. E., Nixon, C. A., Achterberg, R. K., Lavvas, P., Vinatier, S., Teanby, N. A., Bjoraker, G. L., Carlson, R. C., Piani, L., Flasar, F. M., Romani, P. N., 2010. Titan trace gaseous composition from CIRS at the end of the Cassini-Huygens prime mission. Icarus 207, 461–476.

Crespin, A., Lebonnois, S., Vinatier, S., Bézard, B., Coustenis, A., Teanby, N. A., Achterberg, R. K., Rannou, P., Hourdin, F., 2008. Diagnostics of Titan's stratospheric dynamics using Cassini/CIRS data and the 2-dimensional IPSL circulation model. Icarus 197, 556–571.

Eliassen, A., 1951. Slow thermally or frictionally controlled meridional circulation in a circular vortex. Astrophys. Norv. 5, 19–60.

Fels, S. B., 1982. A parameterization of scale-dependent radiative damping rates in the middle atmosphere. J. Atmos. Sci. 39, 1141–1152.

Flasar, F. M., Conrath, B. J., 1990. Titan's stratospheric temperatures - A case for dynamical inertia? Icarus 85, 346–354.

Flasar, F. M., Samuelson, R. E., Conrath, B. J., 1981. Titan's atmosphere - Temperature and dynamics. Nature 292, 693–698.

Flasar, F. M., Kunde, V. G., Abbas, M. M., Achterberg, R. K., Ade, P., Barucci, A., Bézard, B., Bjoraker, G. L., Brasunas, J. C., Calcutt, S., Carlson, R., Césarsky, C. J., Conrath, B. J., Coradini, A., Courtin, R., Coustenis, A., Edberg, S., Edgington, S., Ferrari, C., Fouchet, T., Gautier, D., Gierasch, P. J., Grossman, K., Irwin, P., Jennings, D. E., Lellouch, E., Mamoutkine, A. A., Marten, A., Meyer, J. P., Nixon, C. A., Orton, G. S., Owen, T. C., Pearl, J. C., Prangé, R., Raulin, F., Read, P. L., Romani, P. N., Samuelson, R. E., Segura, M. E., Showalter, M. R., Simon-Miller, A. A., Smith, M. D., Spencer, J. R., Spilker, L. J., Taylor, F. W., 2004. Exploring the Saturn system in the thermal infrared: The Composite Infrared Spectrometer. Space Sci. Rev. 115, 169–297.

Flasar, F. M., Achterberg, R. K., Conrath, B. J., Gierasch, P. J., Kunde, V. G., Nixon, C. A., Bjoraker, G. L., Jennings, D. E., Romani, P. N., Simon-Miller, A. A., Bézard, B., Coustenis, A., Irwin, P. G. J., Teanby, N. A., Brasunas, J., Pearl, J. C., Segura, M. E., Carlson, R. C., Mamoutkine, A., Schinder, P. J., Barucci, A., Courtin, R., Fouchet, T., Gautier, D., Lellouch, E., Marten, A., Prangé, R., Vinatier, S., Strobel, D. F., Calcutt, S. B., Read, P. L., Taylor, F. W., Bowles, N., Samuelson, R. E., Orton, G. S., Spilker, L. J., Owen, T. C., Spencer, J. R., Showalter, M. R., Ferrari, C., Abbas, M. M., Raulin, F., Edgington, S., Ade, P., Wishnow, E. H., 2005. Titan's atmospheric temperatures, winds, and composition. Science 308, 975–978.

Folkner, W. M., Asmar, S. W., Border, J. S., Franklin, G. W., Finley, S. G., Gorelik, J., Johnston, D. V., Kerzhanovich, V. V., Lowe, S. T., Preston, R. A., Bird, M. K., Dutta-Roy, R., Allison, M., Atkinson, D. H., Edenhofer, P., Plettemeier, D., Tyler, G. L., 2006. Winds on Titan from ground-based tracking of the Huygens probe. J. Geophys. Res. 111, E07S02.

Friedson, A. J., West, R. A., Wilson, E. H., Oyafuso, F., Orton, G. S., December 2009. A global climate model of Titan's atmosphere and surface. Planet. Space Sci. 57, 1931–1949.

Houghton, J. T., 1977. The physics of atmospheres. Cambridge University Press.

Hourdin, F., Lebonnois, S., Luz, D., Rannou, P., 2004. Titan's stratospheric composition driven by condensation and dynamics. J. Geophys. Res. 109, 12005–+.

Hourdin, F., Talagrand, O., Sadourny, R., Courtin, R., Gautier, D., McKay, C. P.,

1995. Numerical simulation of the general circulation of the atmosphere of Titan. Icarus 117, 358–374.

Jacquinet-Husson, N., Scott, N. A., Chedin, A., Garceran, K., Armante, R., Chursin, A. A., Barbe, A., Birk, M., Brown, L. R., Camy-Peyret, C., Claveau, C., Clerbaux, C., Coheur, P. F., Dana, V., Daumont, L., Debacker-Barilly, M. R., Flaud, J. M., Goldman, A., Hamdouni, A., Hess, M., Jacquemart, D., Kopke, P., Mandin, J. Y., Massie, S., Mikhailenko, S., Nemtchinov, V., Nikitin, A., Newnham, D., Perrin, A., Perevalov, V. I., Regalia-Jarlot, L., Rublev, A., Schreier, F., Schult, I., Smith, K. M., Tashkun, S. A., Teffo, J. L., Toth, R. A., Tyuterev, V. G., Vander Auwera, J., Varanasi, P., Wagner, G., 2005. The 2003 edition of the GEISA/IASI spectroscopic database. J. Quant. Spectro. Rad. Trans. 95, 429–467.

Lacis, A. A., Oinas, V., 1991. A description of the correlated-k distribution method for modelling nongray gaseous absorption, thermal emission, and multiple scattering in vertically inhomogeneous atmospheres. J. Geophys. Res. 96 (15), 9027–9064.

Lebonnois, S., Toublanc, D., Hourdin, F., Rannou, P., 2001. Seasonal Variations of Titan's Atmospheric Composition. Icarus 152, 384–406.

Lebonnois, S., Hourdin, F., Rannou, P., Luz, D., Toublanc, D., 2003. Impact of the seasonal variations of composition on the temperature field of Titan's stratosphere. Icarus 163, 164–174.

Lebonnois, S., Rannou, P., Hourdin, F., 2009. The coupling of winds, aerosols and chemistry in Titan's atmosphere. Phil. Trans. R. Soc. A 367, 665–682.

Luz, D., Hourdin, F., Dec. 2003. Latitudinal transport by barotropic waves in Titan's stratosphere. I. General properties from a horizontal shallow-water model. Icarus 166, 328–342.

Luz, D., Hourdin, F., Rannou, P., Lebonnois, S., Dec. 2003. Latitudinal transport by barotropic waves in Titan's stratosphere. II. Results from a coupled dynamics-microphysics-photochemistry GCM. Icarus 166, 343–358.

Montgomery, M. T., Shapiro, L. J., 1995. Generalized Charney-Stern and Fjortoft theorems for rapidly rotating vortices. J . Atmos. Sci. 52, 1829–1833.

Niemann, H. B., Atreya, S. K., Bauer, S. J., Carignan, G. R., Demick, J. E., Frost, R. L., Gautier, D., Haberman, J. A., Harpold, D. N., Hunten, D. M., Israel, G., Lunine, J. I., Kasprzak, W. T., Owen, T. C., Paulkovich, M., Raulin, F., Raaen, E., Way, S. H., 2005. The abundances of constituents of Titan's atmosphere from the GCMS instrument on the Huygens probe. Nature 438, 779–784.

Pierrehumbert, R. T., Swanson, K. L., 1995. Baroclinic instability. Ann. Rev. Fluid. Mech. 27, 419–467.

Press, W. H., Teukolsky, S. A., 1988. Search algorithm for weak periodic signals in unevenly spaced data. Computers in Physics 2, 77–82.

Rannou, P., Hourdin, F., McKay, C. P., Luz, D., 2004. A coupled dynamics-microphysics model of Titan's atmosphere. Icarus 170, 443–462.

Rannou, P., Lebonnois, S., Hourdin, F., Luz, D., 2005. Titan atmosphere database. Adv. Space Res. 36, 2194–2198.

Roman, M. T., West, R. A., Banfield, D. J., Gierasch, P. J., Achterberg, R. K., Nixon, C. A., Thomas, P. C., 2009. Determining a tilt in Titan's north-south albedo asymmetry from Cassini images. Icarus 203, 242–249.

Smith, B. A., Soderblom, L., Beebe, R. F., Boyce, J. M., Briggs, G., Bunker, A., Collins, S. A., Hansen, C., Johnson, T. V., Mitchell, J. L., Terrile, R. J., Carr, M. H., Cook, A. F., Cuzzi, J. N., Pollack, J. B., Danielson, G. E., Ingersoll, A. P., Davies, M. E., Hunt, G. E., Masursky, H., Shoemaker, E. M., Morrison, D., Owen, T., Sagan, C., Veverka, J., Strom, R., Suomi, V. E., 1981. Encounter with Saturn - Voyager 1 imaging science results. Science 212, 163–191.

Strobel, D. F., 2009. Titan's hydrodynamically escaping atmosphere: Escape rates and the structure of the exobase region. Icarus 202, 632–641.

Strobel, D. F., Atreya, S. K., Bézard, B., Ferri, F., Flasar, F. M., Fulchignoni, M., Lellouch, E., Müller-Wodarg, I., 2009. Atmosperic structure and composition. In: Brown, R. H., Lebreton, J.-P., Waite, J. H. (Eds.), Titan from Cassini-Huygens. Springer, Dordrecht, Ch. 10, pp. 235–257.

Teanby, N. A., Irwin, P. G. J., de Kok, R., Nixon, C. A., Coustenis, A., Royer, E., Calcutt, S. B., Bowles, N. E., Fletcher, L., Howett, C., Taylor, F. W., 2008. Global and temporal variations in hydrocarbons and nitriles in Titan's stratosphere for northern winter observed by Cassini/CIRS. Icarus 193, 595–611.

Teanby, N. A., Irwin, P. G. J., de Kok, R., Nixon, C. A., 2009. Dynamical implications of seasonal and spatial variations in Titan's stratospheric composition. Phil. Trans. R. Soc. A 367, 697–711.

Teanby, N. A., Irwin, P. G. J., de Kok, R., 2010. Compositional evidence for Titan's stratospheric tilt. Planet. Space Sci. 58, 792–800.

Tokano, T., 2010. Westward rotation of the atmospheric angular momentum vector of Titan by thermal tides. Planet. Space Sci. 58, 814–829.

Tokano, T., Neubauer, F. M., Laube, M., McKay, C. P., 1999. Seasonal variation of Titan's atmospheric structure simulated by a general circulation model. Planet. Space Sci. 47, 493–520.

Tomasko, M. G., Bézard, B., Doose, L., Engel, S., Karkoschka, E., Vinatier, S., 2008. Heat balance in Titan's atmosphere. Planet. Space Sci. 56, 648–659.

Table 1: Summary of Nadir Observations

Encounter	Start Time	Duration (h:mm)	Latitude Range	No. of Spectra	Resolution (° of arc)	L_S °
T0	2004 Jul 02 03:30:21	13:30	88° S - 29° N	4497	2.1	293
TB	2004 Dec 13 15:12:29	8:25	84° S - 67° N	2405	2.1	299
T3	2005 Feb 14 09:57:53	9:00	79° S - 71° N	2354	2.1	301
T3	2005 Feb 15 18:57:53	4:20	73° S - 77° N	1585	1.8	301
T4	2005 Apr 01 08:05:16	6:30	76° S - 74° N	2230	1.9	303
T6	2005 Aug 22 20:53:37	6:47	83° S - 66° N	2126	1.9	308
T8	2005 Oct 27 01:24:00	7:00	74° S - 74° N	3436	2.9	311
T8	2005 Oct 28 16:15:25	7:49	75° S - 73° N	1915	1.9	311
T9	2005 Dec 27 14:04:00	10:07	74° S - 74° N	4032	2.9	313
T10	2006 Jan 14 14:23:27	9:13	77° S - 76° N	2741	2.1	314
T14	2006 May 21 01:18:11	2:00	8° N - 77° N	1353	1.7	318
T14	2006 May 21 06:18:11	2:58	68° S - 42° N	1900	2.4	318
T15	2006 Jul 02 23:50:47	7:54	75° S - 75° N	1862	2.3	320
T17	2006 Sep 06 21:56:51	7:20	66° S - 83° N	2102	2.4	322
T18	2006 Sep 22 20:58:49	7:00	63° S - 87° N	1705	2.3	323
T19	2006 Oct 08 20:16:07	6:14	56° S - 88° N	4520	2.2	323
T21	2006 Dec 11 16:02:17	4:03	45° S - 88° N	1248	2.1	326
T22	2006 Dec 27 15:04:13	4:56	38° S - 89° N	3336	2.0	326
T23	2007 Jan 12 14:23:31	2:15	31° S - 52° N	874	2.1	327
T23	2007 Jan 12 17:38:31	2:00	6° N - 89° N	1912	1.7	327
T23	2007 Jan 13 22:38:31	3:24	88° S - 25° N	1503	1.9	327
T24	2007 Jan 28 13:00:55	2:15	5° N - 89° N	1840	2.1	327
T24	2007 Jan 29 21:15:55	5:14	89° S - 21° N	3654	1.9	327
T26	2007 Mar 09 11:08:00	1:41	89° S - 25° S	1935	1.8	329
T27	2007 Mar 25 09:07:27	2:16	88° S - 7° S	2444	1.8	329
T28	2007 Apr 11 12:58:00	7:14	46° S - 88° N	2357	2.2	330
T30	2007 May 12 05:45:58	1:24	88° S - 55° N	1187	1.8	331
T30	2007 May 13 10:09:58	1:19	60° S - 85° N	1123	1.9	331
T32	2007 Jun 14 07:46:11	2:15	2° S - 79° N	1785	1.9	332
T34	2007 Jul 18 01:48:20	7:23	74° S - 73° N	2273	2.7	334
T35	2007 Aug 13 21:32:34	6:00	70° S - 64° N	750	2.1	335
T36	2007 Oct 02 18:42:43	8:46	67° S - 72° N	3943	5.3	336
T37	2007 Nov 19 14:47:25	7:00	71° S - 81° N	3848	2.3	338
T38	2007 Dec 05 14:06:50	9:37	64° S - 87° N	6943	2.4	339
T40	2008 Jan 06 11:30:20	7:00	54° S - 88° N	3878	2.3	340
T41	2008 Feb 23 12:32:07	2:53	46° S - 89° N	2143	2.7	341
T43	2008 May 13 02:46:58	6:30	48° S - 89° N	5255	2.6	344
T44	2008 May 27 10:24:32	6:00	88° S - 48° N	2289	2.5	345
T45	2008 Jul 30 08:05:21	4:07	89° S - 49° N	2903	2.0	347
T48	2008 Dec 06 05:56:28	3:06	38° S - 89° N	2733	2.0	351
T49	2008 Dec 20 17:24:32	6:35	89° S - 37° N	3034	2.0	352
T49	2008 Dec 22 02:29:52	3:30	31° S - 89° N	2884	1.9	352
T51	2009 Mar 26 11:00:31	3:43	89° S - 22° N	2661	2.0	355
T51	2009 Mar 27 18:13:36	5:12	17° S - 89° N	4110	2.0	355
T52	2009 Apr 03 10:29:34	1:48	87° S - 18° N	586	2.1	356
T52	2009 Apr 04 15:47:47	7:37	31° N - 89° N	2427	1.7	356
T54	2009 May 05 08:11:47	4:42	20° S - 89° N	4163	1.5	357
T55	2009 May 21 07:09:49	1:17	24° S - 89° N	1274	1.7	357
T55	2009 May 22 11:26:41	8:00	89° S - 25° N	4264	2.2	357
T57	2009 Jun 23 08:32:35	8:00	89° S - 42° N	5085	2.2	358
T59	2009 Jul 23 23:34:04	3:00	51° S - 89° N	2484	1.8	359
T62	2009 Oct 11 15:15:21	4:21	70° S - 72° N	1055	1.9	2
T63	2009 Dec 12 15:03:04	5:00	74° S - 73° N	1996	2.0	4

Table 2: Summary of Limb Observations

Encounter	Start Time	Duration (h:mm)	Latitude Range	Mean Longitude (° West)	Vertical Resolution (km)	L_S °
T04	2005 Apr 01 00:25:12	3:30	3° N - 86° N	132	35	303
T06	2005 Aug 22 01:10:00	2:30	34° S - 26° N	295	35	308
T06	2005 Aug 22 13:40:00	2:30	80° S - 38° S	318	35	308
T08	2005 Oct 27 09:38:09	3:20	11° N - 86° N	72	40	311
T13	2006 Apr 30 11:53:31	5:00	1° N - 41° N	99	28	318
T16	2006 Jul 22 05:25:13	2:15	31° N - 76° N	56	33	320
T20	2006 Oct 25 20:28:07	3:00	14° S - 51° N	35	33	324
T26	2007 Mar 09 16:49:00	4:00	31° S - 30° N	305	40	329
T32	2007 Jun 13 08:46:11	4:00	79° S - 15° N	285	40	332
T37	2007 Nov 18 15:47:25	4:00	88° S - 21° S	158	41	338
T39	2007 Dec 21 13:57:55	3:54	24° S - 74° N	99	41	339
T42	2008 Mar 25 19:27:48	4:00	56° S - 16° S	179	41	342
T45	2008 Jul 31 06:58:11	3:30	1° S - 44° N	190	37	347
T54	2009 May 05 13:54:16	3:50	21° S - 31° N	195	39	357
T59	2009 Jul 24 06:34:04	4:00	1° S - 59° N	245	40	359
T63	2009 Dec 11 16:03:14	4:00	1° S - 83° N	107	39	4

Figure Captions

Figure 1. Latitude and time coverage of the nadir (top) and limb (bottom) temperature mapping observations.

Figure 2. (*top*) Zonal mean temperatures, determined from both nadir and limb data, averaged over the time period from July 2004 through March 2006 (T0-T13 flybys). Temperatures were averaged in 5° latitude bins, then smoothed with a 10° boxcar function applied three times. Contours are labeled in K. The retrieved temperatures are valid over the pressure range between about 0.005 and 8 mbar, except poleward of 60° N, where they are valid between about 0.005 and 2 mbar. (*bottom*) As the top panel, but averaged over the time period from July 2008 to December 2009 (T45-T63 flybys). (*middle*) Difference in zonal mean temperature between the lower and upper panels.

Figure 3. Northern hemispheric temperatures retrieved from all individual limb temperature maps with nearly complete northern hemisphere coverage. The dashed line indicates the stratopause, calculated as the pressure corresponding to the temperature maximum at each latitude.

Figure 4. Equatorial temperatures retrieved from all individual limb temperature maps with nearly complete coverage between 30° S and 30° N. The dashed line indicates the stratopause, calculated as the pressure corresponding to the temperature maximum at each latitude.

Figure 5. Southern hemisphere temperatures retrieved from all individual limb temperature maps with nearly complete southern hemisphere coverage. The dashed line indicates the stratopause, calculated as the pressure corresponding to the temperature maximum at each latitude.

Figure 6. Retrieved 1 mbar temperatures, zonally averaged in 5° wide latitude bins from individual nadir maps, as a function of time. (*top*) Temperatures at 60° N

(blue squares), 70° N (red circles) and 80° N (black crosses). (*middle*) Temperatures as 30° S (blue squares), equator (black crosses) and 30° N (red circles). (*bottom*) Temperatures at 45° S (green diamonds), 60° S (blue squares), 75° S (red circles) and 85° S (black crosses).

Figure 7. Zonal winds calculated from the temperature averages in figure 2 using the gradient wind equation, assuming solid body rotation at the 10 mbar level at four times Titan's rotation rate. Wind speed contours (black lines) are labeled in m s^{-1}. (*top*) Zonal winds from temperatures over the time period from July 2004 through March 2006 (T0-T13 flybys). Temperatures were averaged in 5° latitude bins, then smoothed with a 10° boxcar function applied three times. Contours are labeled in K. (*bottom*) As the top panel, but for the time period from July 2008 to December 2009 (T45-T63 flybys). (*middle*) Difference in zonal winds between the lower and upper panels.

Figure 8. Least squares fits to the symmetry axis of the 1 mbar temperatures from nadir data from individual flybys. The left column show the fits in a sun-fixed reference frame, the right column in a star-fixed (inertial) reference frame. The top panels show the fitted azimuth of the pole fit as a function of time, the bottom panels show the amplitude of the offset from the IAU defined pole as a function of time. The dotted lines are least-squares fits to a linear variation with time.

Figure 9. Temperatures at 0.4 mbar (red) and 1.0 mbar (blue) from Voyager 1 IRIS retrievals of Flasar and Conrath (1990) (points) and from CIRS data averaged over the period between June 2008 and June 2009 (lines).

Figure 10. Results from a Laboratoire de Météorologie Dynamique (LMD) 2-D circulation model taken from http://www.lmd.jussieu.fr/titanDbase/index.hml (Rannou et al., 2005). The three panels on the left show meridional cross sections of temperature for $L_s = 309°$ (top), $L_s = 358°$ (bottom), and the change in temperature between

the two time periods (middle). The three right-hand panels show similar results for the zonal wind.

Figure 11. Potential temperature calculated from the temperature averages in figure 2. The top panel is from data averaged from July 2004 through March 2006, the bottom panel is from data averaged from July 2008 through December 2009. The middle panel is the difference between the bottom and top panels. Contours are labeled in K.

Figure 12. Zonal angular momentum calculated from the temperature averages in figure 2. The top panel is from data averaged from July 2004 through March 2006, the bottom panel is from data averaged from July 2008 through December 2009. The middle panel is the difference between the bottom and top panels. Contours are labeled in units of $10^6 \mathrm{m}^2\,\mathrm{s}^{-1}$.

Figure 13. Ertel potential vorticity calculated from the temperature averages in figure 2. The top panel is from data averaged from July 2004 through March 2006, the bottom panel is from data averaged from July 2008 through December 2009. The middle panel is the difference between the bottom and top panels. Contours are labeled in $\mathrm{m}^2\,\mathrm{K}\,\mathrm{kg}^{-1}\,\mathrm{s}^{-1}$.

Figure 14. Estimates of the radiative cooling timescales at 5° S (solid line) and 75° N (dashed line).

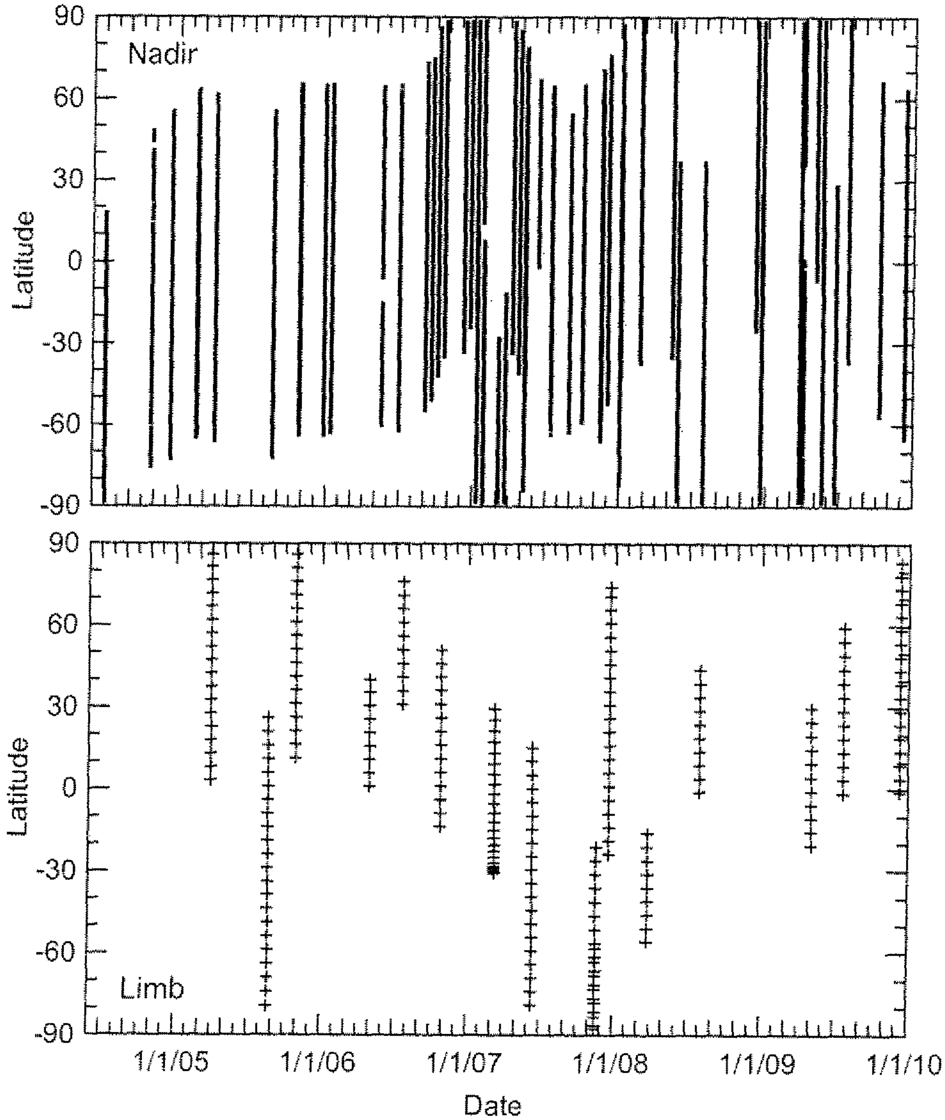

Nadir
Limb
90
60
30
0
-30
-60
-90
Latitude
1/1/05
1/1/06
1/1/07
1/1/08
1/1/09
1/1/10
Date

Figure 1:

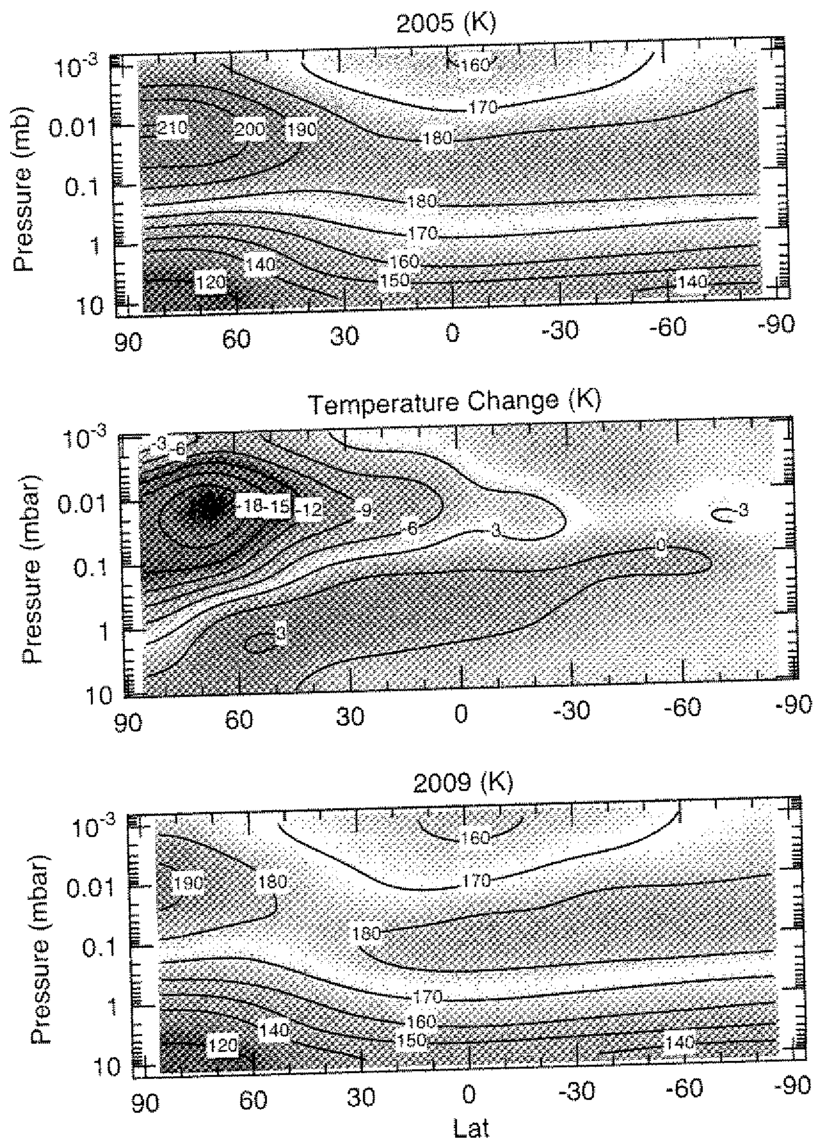
2005 (K)
Pressure (mb)
Temperature Change (K)
Pressure (mbar)
2009 (K)
Pressure (mbar)
Lat

Figure 2:

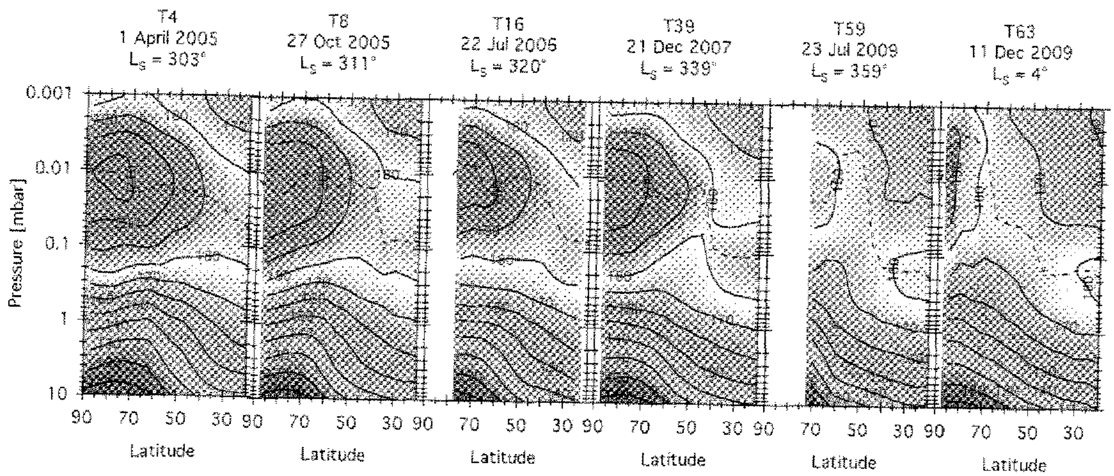
T4
1 April 2005
L_s = 303°
T8
27 Oct 2005
L_s = 311°
T16
22 Jul 2006
L_s = 320°
T39
21 Dec 2007
L_s = 339°
T59
23 Jul 2009
L_s = 359°
T63
11 Dec 2009
L_s = 4°
Pressure [mbar]
0.001
0.01
0.1
1
10
90 70 50 30
Latitude

Figure 3:

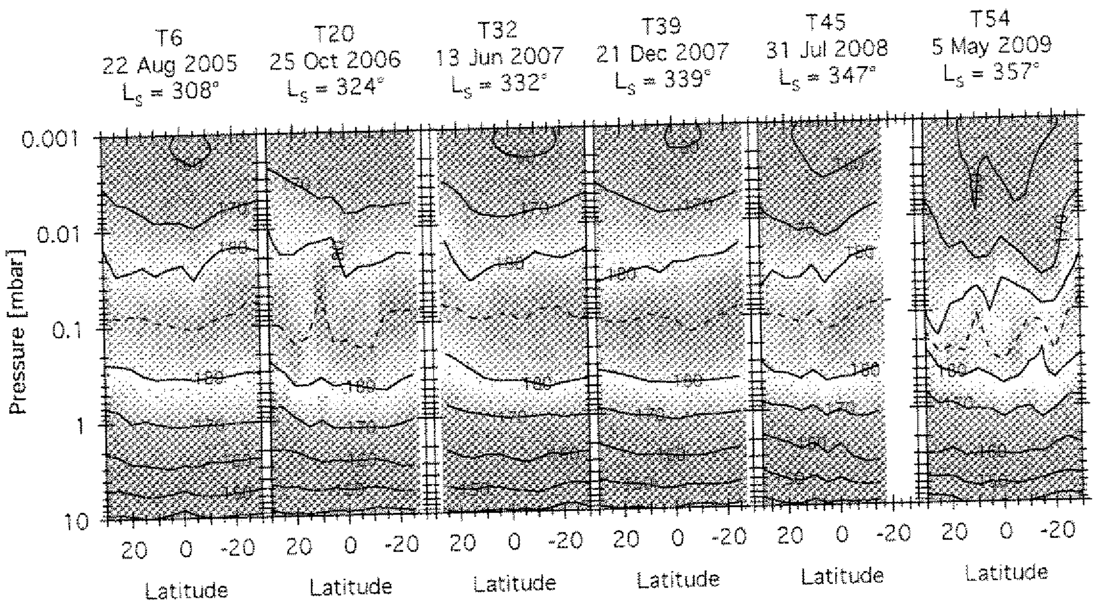
T6
22 Aug 2005
L_s = 308°
T20
25 Oct 2006
L_s = 324°
T32
13 Jun 2007
L_s = 332°
T39
21 Dec 2007
L_s = 339°
T45
31 Jul 2008
L_s = 347°
T54
5 May 2009
L_s = 357°
Pressure [mbar]
0.001
0.01
0.1
1
10
20 0 -20
Latitude

Figure 4:

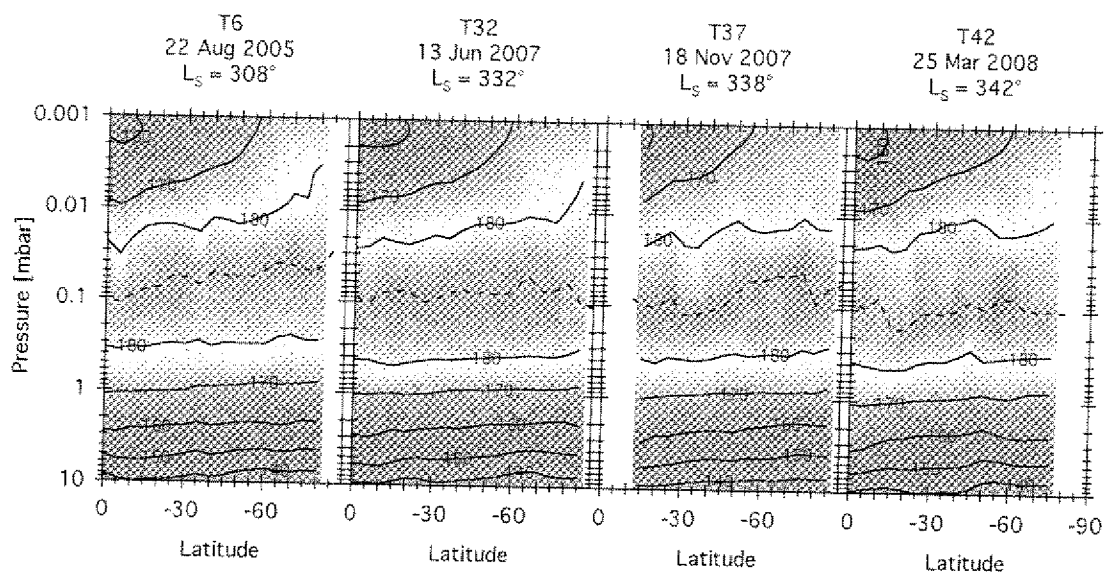
T6
22 Aug 2005
L_S = 308°
T32
13 Jun 2007
L_S = 332°
T37
18 Nov 2007
L_S = 338°
T42
25 Mar 2008
L_S = 342°
Pressure [mbar]
0.001
0.01
0.1
1
10
0
-30
-60
-90
Latitude
180
170
160
150

Figure 5:

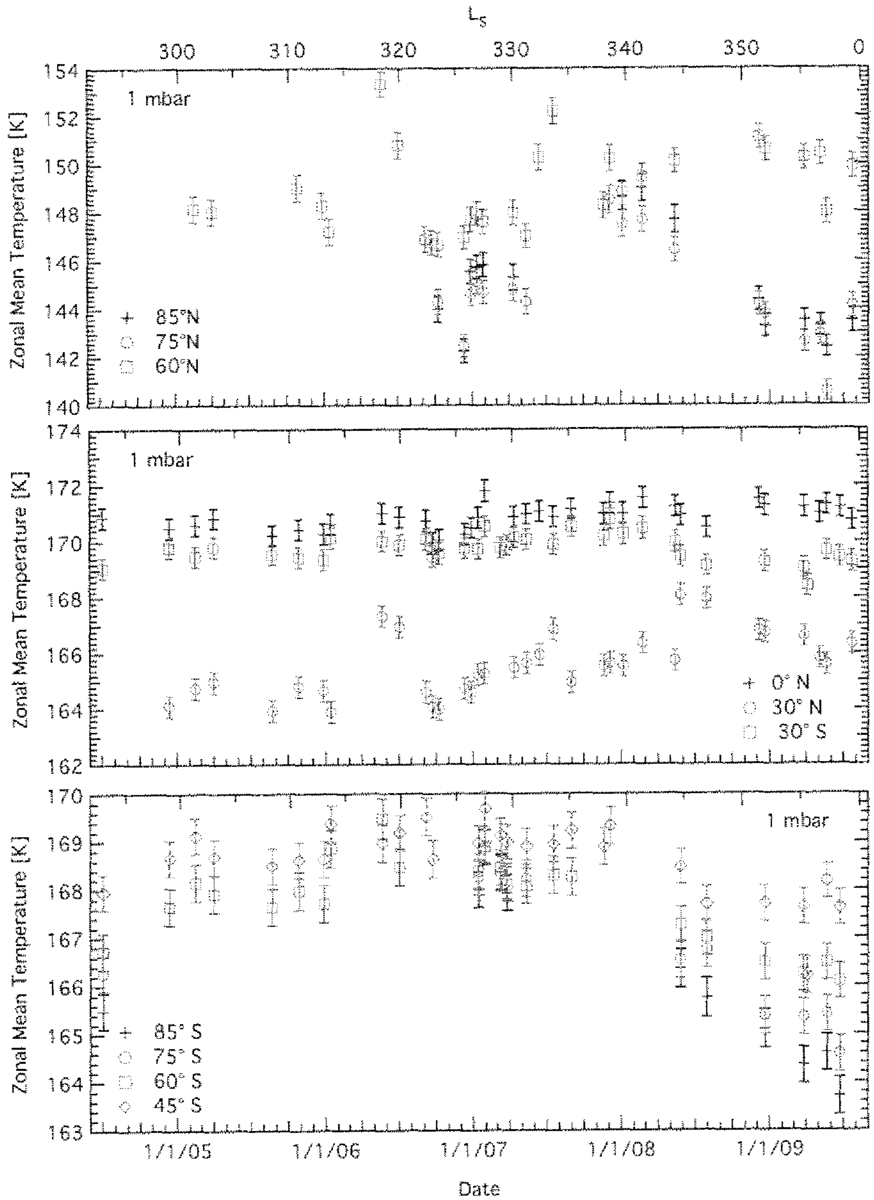

L_S
300
310
320
330
340
350
0
Zonal Mean Temperature [K]
1 mbar
+ 85°N
○ 75°N
□ 60°N
+ 0° N
○ 30° N
□ 30° S
+ 85° S
○ 75° S
□ 60° S
◇ 45° S
1/1/05
1/1/06
1/1/07
1/1/08
1/1/09
Date

Figure 6:

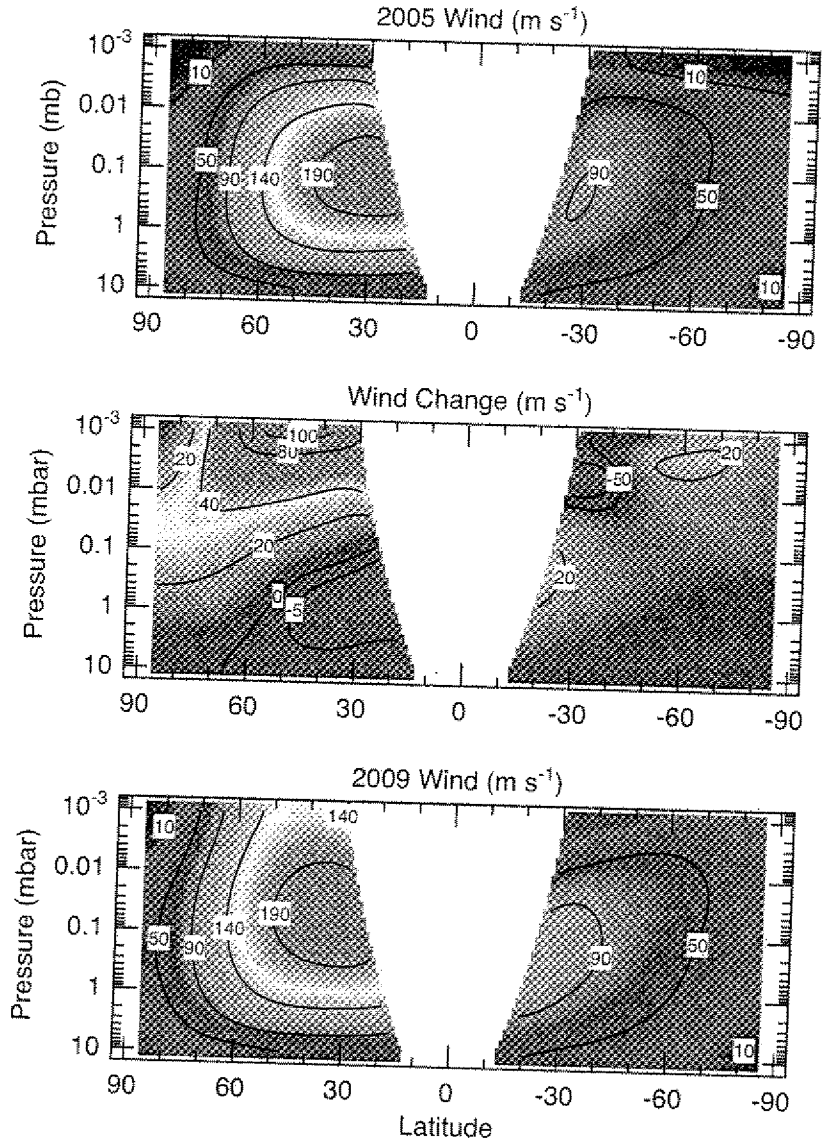
2005 Wind (m s-1)
Pressure (mb)
10-3
0.01
0.1
1
10
10
50
90
140
190
90
50
10
10
90
60
30
0
-30
-60
-90
Wind Change (m s-1)
Pressure (mbar)
10-3
0.01
0.1
1
10
100
80
20
40
20
0
-5
-50
20
20
90
60
30
0
-30
-60
-90
2009 Wind (m s-1)
Pressure (mbar)
10-3
0.01
0.1
1
10
10
140
190
140
50
90
90
50
10
90
60
30
0
-30
-60
-90
Latitude

Figure 7:

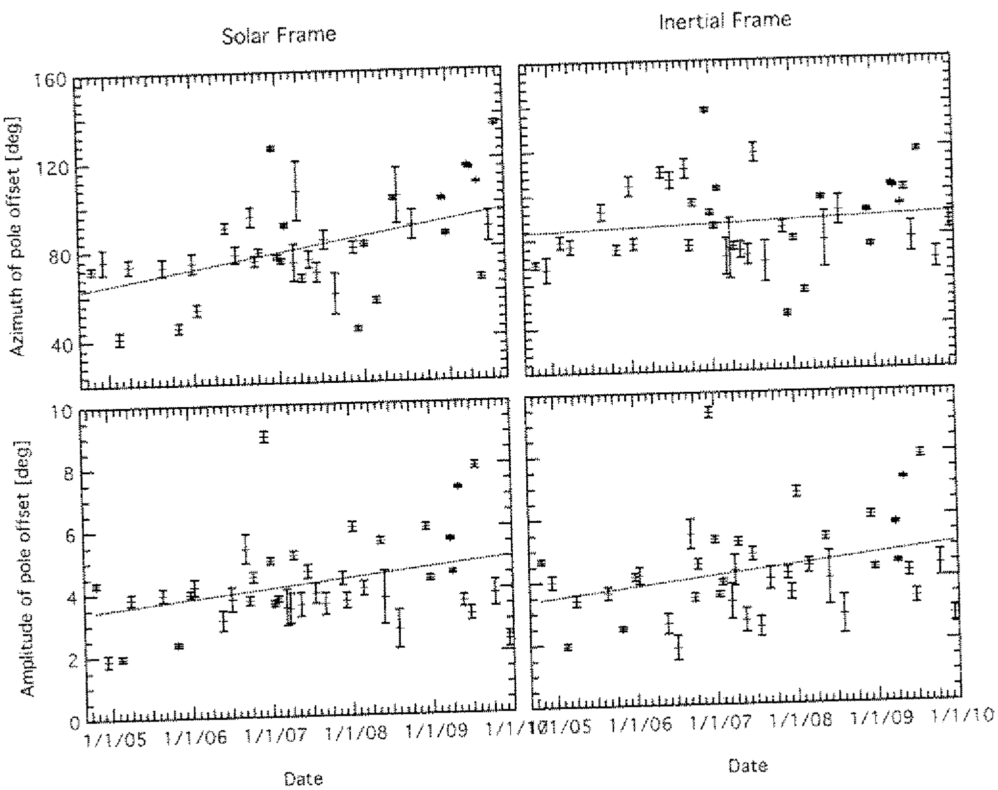
Solar Frame
Inertial Frame
Azimuth of pole offset [deg]
Amplitude of pole offset [deg]
160
120
80
40
10
8
6
4
2
0
1/1/05
1/1/06
1/1/07
1/1/08
1/1/09
1/1/10
Date
Date

Figure 8:

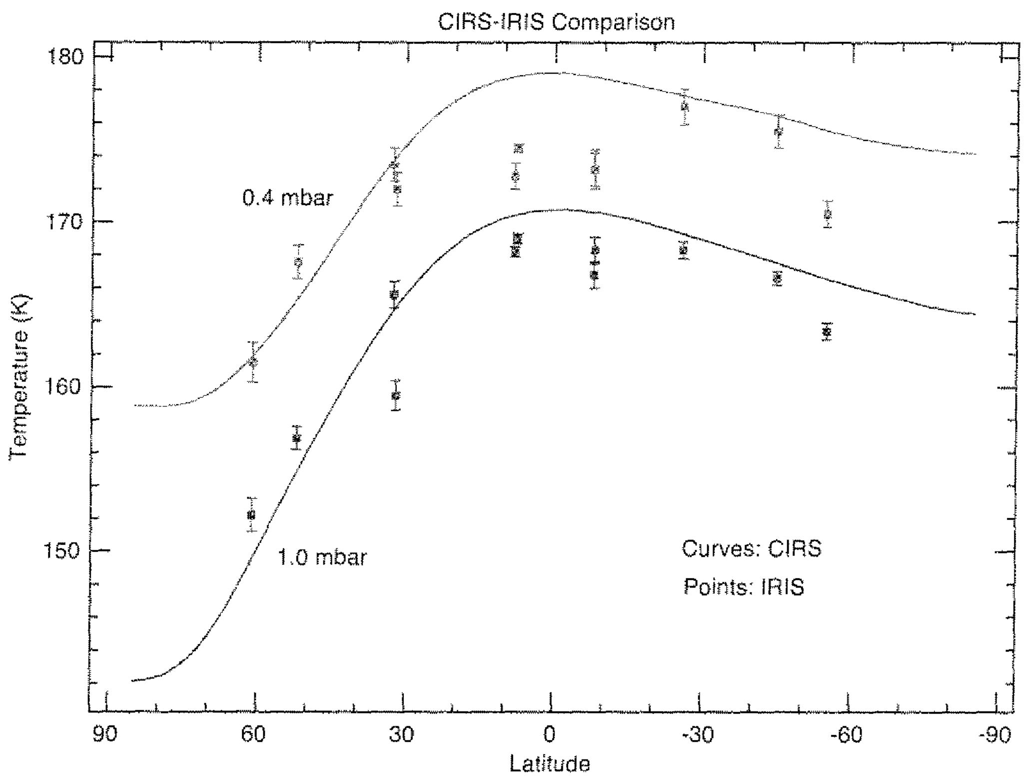
CIRS-IRIS Comparison
180
170
160
150
Temperature (K)
0.4 mbar
1.0 mbar
Curves: CIRS
Points: IRIS
90
60
30
0
-30
-60
-90
Latitude

Figure 9:

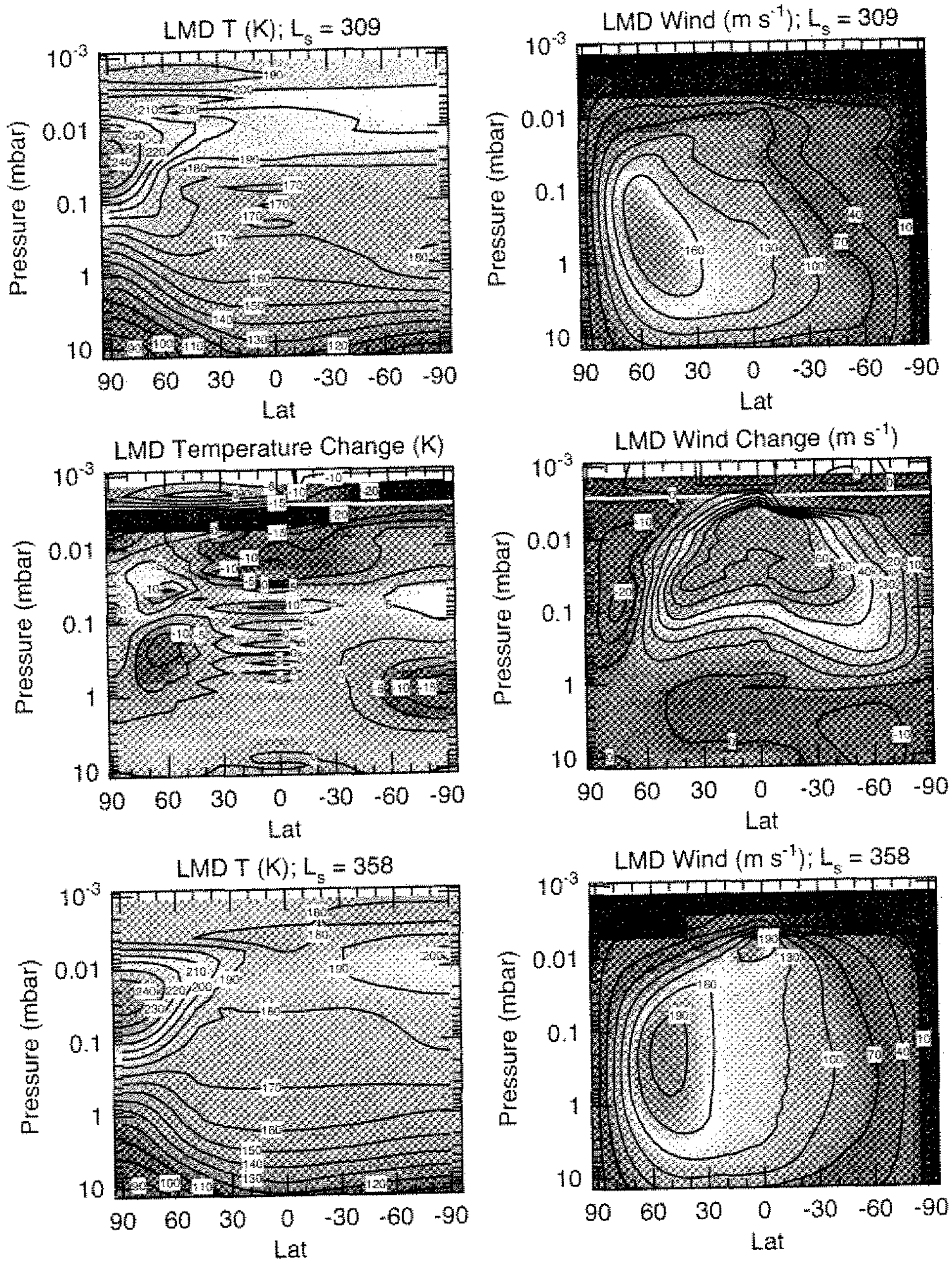
LMD T (K); L$_s$ = 309
LMD Wind (m s^{-1}); L$_s$ = 309
LMD Temperature Change (K)
LMD Wind Change (m s^{-1})
LMD T (K); L$_s$ = 358
LMD Wind (m s^{-1}); L$_s$ = 358
Pressure (mbar)
Lat

Figure 10:

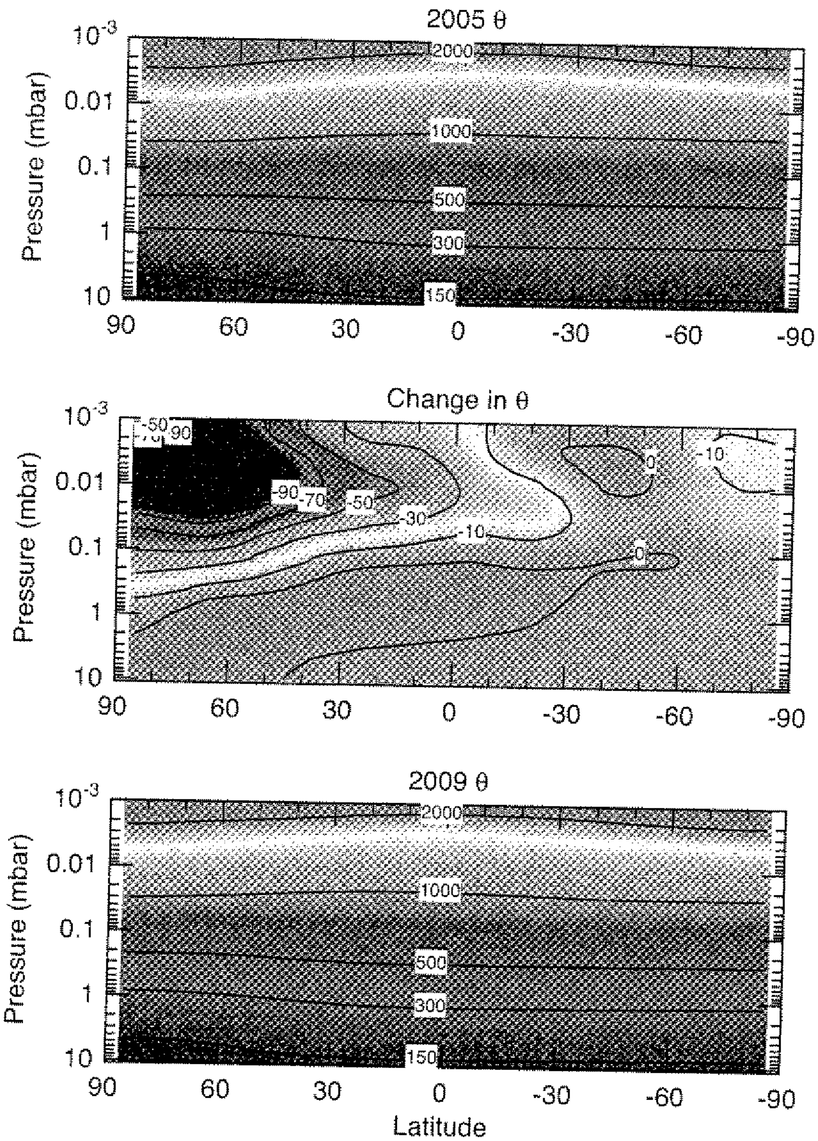
2005 θ
Pressure (mbar)
2000
1000
500
300
150
Change in θ
-50
90
-90
-70
-50
-30
-10
0
-10
0
2009 θ
2000
1000
500
300
150
Latitude

Figure 11:

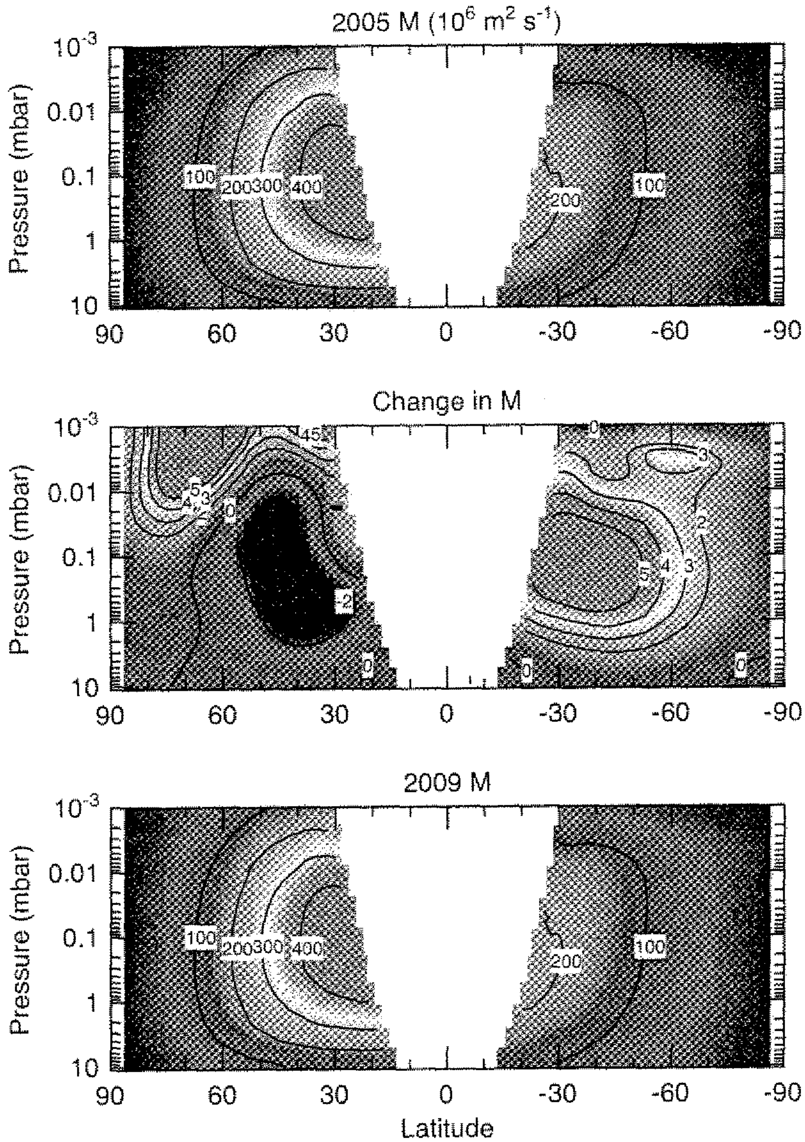

2005 M (10^6 m^2 s^{-1})
Pressure (mbar)
10^{-3}
0.01
0.1
1
10
90
60
30
0
-30
-60
-90
100
200
300
400
Change in M
0
2
3
4
5
-2
2009 M
Latitude

Figure 12:

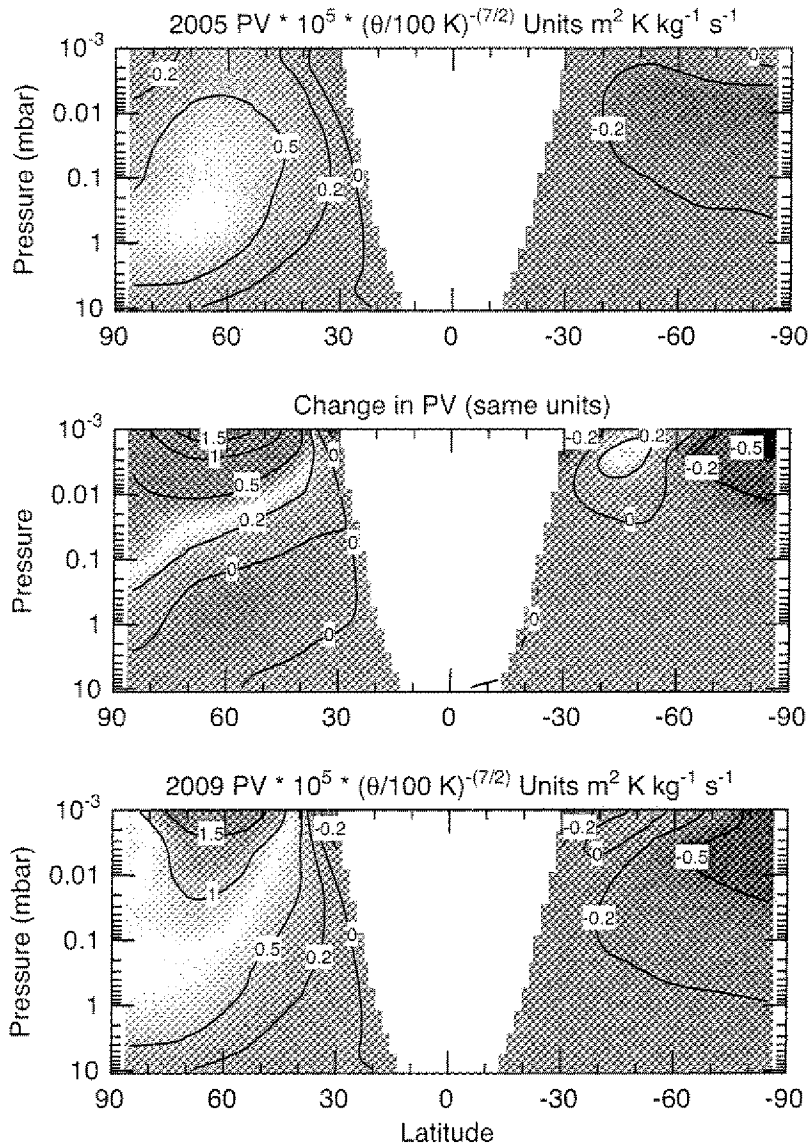
2005 PV * 10^5 * (θ/100 K)^-(7/2) Units m^2 K kg^-1 s^-1
Pressure (mbar)
Change in PV (same units)
Pressure
2009 PV * 10^5 * (θ/100 K)^-(7/2) Units m^2 K kg^-1 s^-1
Pressure (mbar)
Latitude

Figure 13:

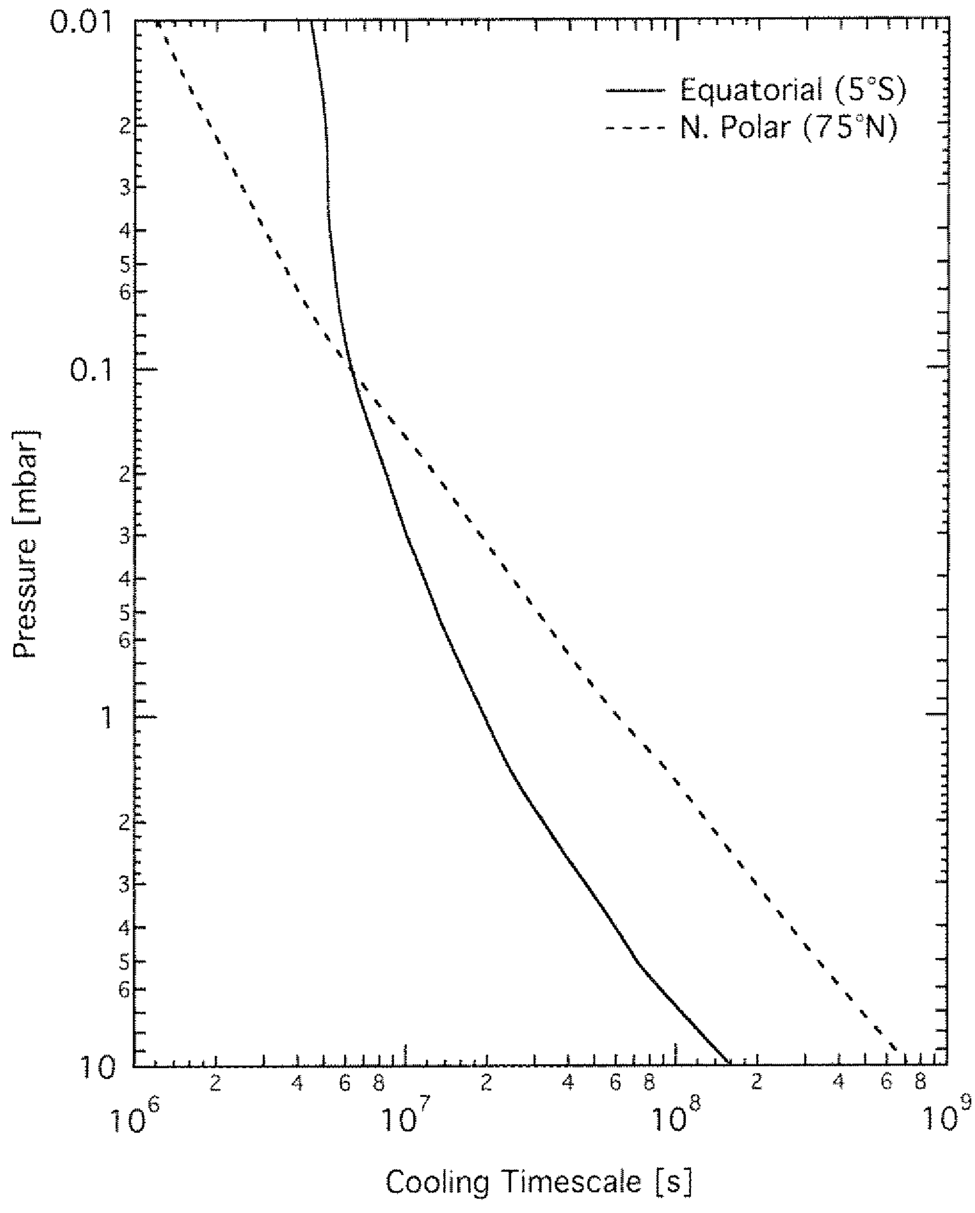
Equatorial (5°S)
N. Polar (75°N)
Pressure [mbar]
0.01
0.1
1
10
Cooling Timescale [s]
10^6
10^7
10^8
10^9

Figure 14: